AIChE
JOURNAL

Thermodynamics of molybdenum trioxide encapsulated in zeolite Y

Xianghui Zhang[1,2] | Andrew C. Strzelecki[1,3,4] | Cody B. Cockreham[1,2,5] |
Vitaliy G. Goncharov[1,3,5] | Houqian Li[2] | Junming Sun[2] | Hui Sun[6,7] |
Xiaofeng Guo[1,3,4] | Hongwu Xu[5] | Ha Su[2] | Baodong Wang[8] |
Yong Wang[2,9] | Di Wu[1,2,3,4]

[1]Alexandra Navrotsky Institute for Experimental Thermodynamics, Washington State University, Pullman, Washington, USA

[2]The Gene and Linda Voiland School of Chemical Engineering and Bioengineering, Washington State University, Pullman, Washington, USA

[3]Department of Chemistry, Washington State University, Pullman, Washington, USA

[4]Materials Science and Engineering, Washington State University, Pullman, Washington, USA

[5]Earth and Environmental Sciences Division, Los Alamos National Laboratory, Los Alamos, New Mexico, USA

[6]Petroleum Processing Research Center, East China University of Science and Technology, Shanghai, China

[7]International Joint Research Center of Green Energy Chemical Engineering, East China University of Science and Technology, Shanghai, China

[8]National Institute of Clean-and-Low-Carbon Energy, Beijing, China

[9]Institute for Integrated Catalysis, Pacific Northwest National Laboratory, Richland, Washington, USA

Correspondence
Di Wu, Alexandra Navrotsky Institute for Experimental Thermodynamics, The Gene and Linda Voiland School of Chemical Engineering and Bioengineering, Washington State University, Pullman, WA 99163, USA.
Email: d.wu@wsu.edu

Abstract

Zeolites with encapsulated transition metal species are extensively applied in the chemical industry as heterogenous catalysts for favorable kinetic pathways. To elucidate the energetic insights into formation of subnano-sized molybdenum trioxide (MoO_3) encapsulated/confined in zeolite Y (FAU) from constituent oxides, we performed a systematic experimental thermodynamic study using high-temperature oxide melt solution calorimetry as the major tool. Specifically, the formation enthalpy of each MoO_3/FAU is less endothermic than corresponding zeolite Y, suggesting enhanced thermodynamic stability. As Si/Al ratio increases, the enthalpies of formation of MoO_3/FAU with identical loading (5 Mo-wt%) tend to be less endothermic, ranging from 61.1 ± 1.8 (Si/Al = 2.9) to 32.8 ± 1.4 kJ/mol TO_2 (Si/Al = 45.6). Coupled with spectroscopic, structural and morphological characterizations, we revealed intricate energetics of MoO_3–zeolite Y guest–host interactions determined by the Si/Al ratio and the subtle redox and/or local structural evolutions of encapsulated MoO_3.

KEYWORDS
colloids (of metal oxide nanoparticles), thermodynamics/classical, zeolites

This study is dedicated to a friend and colleague of Di Wu, Prof. Chia-Kuang (Frank) Tsung, Associate Professor of Chemistry at Boston College, who passed away on January 5, 2021 from complications due to COVID-19.

1 | INTRODUCTION

For the foreseeable future, carbon-based fuels, such as natural gas, petroleum, coal, and biomass, will continue to be a significant part of our energy infrastructure, and interfacially engineered heterogeneous catalytic materials relying on transition metal (TM) species will continue to play a critical role in meeting our daily energy needs.[1-4] It has been demonstrated that supported or confined TMs, their oxide (TMO), carbide (TMC), and nitride (TMN) particles exhibit promising performance with high activity and selectivity in selective conversion of methane,[5-8] low-temperature CO conversion,[9,10] selective hydrogenation/dehydrogenation,[11-14] bio-oil conversion and upgrading,[15-18] and water–gas shift reaction.[19,20] Existing literature on heterogeneous catalytic materials primarily emphasize their outstanding performance and complexity in kinetics and reaction mechanisms. Meanwhile, the rapid development of catalyst synthesis has outran the existing thermodynamic database of materials that mainly documents the thermochemical properties of homogeneous systems, such as solid solutions.[21] There are currently no systematic experimental thermodynamic data on the formation energetics of interfacially supported and spatially confined/encapsulated TM species that feature solid–solid interfaces and grain boundaries.[21] Moreover, the energetics of such particle–support or guest–host interfacial interactions, put simply, "the energetic cost of being small", is unknown.[21] The long-term goal of our group is to narrow such widening knowledge gap by carrying out thermodynamic studies on materials with interfacially stabilized subnano clusters and nanoparticles using calorimetry as the fundamental tool. We expect that such experimentally determined energetic insights will enable enhanced understanding for further development of inexpensive and more sustainable energy harvesting and conversion materials, nanostructured catalysts and sorbents using earth-abundant elements.

The current focus of our group is on thermodynamics of zeolites with encapsulated TM-based particles/clusters. Zeolites are framework aluminosilicates with open microporosity constructed by corner-sharing tetrahedron units, in which the T atom is silicon (Si) or aluminum (Al). Substitution of Si^{4+} by Al^{3+} enables negatively charged framework structures with Brønsted and Lewis acidity. Owing to their crystalline open framework topologies and tunable surface sites, zeolites offer ideal platforms to support TM species for heterogeneous catalysis with high activity and shape selectivity.[22,23] Employing a suite of highly customized calorimeters, in collaboration with Drs. Davis and Zones, the Navrotsky Group pioneered research on thermodynamics of pure zeolites since 1990s, in which the cation–water–zeolite interplays of alkali and alkaline earth ion-exchanged zeolites, organic structural directing agent (OSDA)–framework interactions, formation mechanisms under hydrothermal/solvothermal synthesis, and adsorption energetics of small molecules, such as water, CO_2, and organics, were systematically investigated.[24-41] The general conclusions are as follows: (i) dehydrated zeolites are moderately metastable compared with their dense phase assemblages by less than 15 kJ/mol per TO_2 unit, and as the framework molar volume increases, such energetic

difference tends to be more significant. The energetic stability of dehydrated alkali and alkaline earth ion-exchanged aluminosilicate zeolites is a complex function of Si/Al ratio and charge-balancing cations. (ii) Generally, hydration or adsorption of small organics is exothermic and tends to be less negative as the adsorbate loading increases. (iii) Similarly, the energetics of OSDA—framework interactions and zeolite formation energetics under hydrothermal condition suggest moderately exothermic bonding, a product of subtly balanced enthalpy and entropy factors.[24-41] These studies have laid a solid foundation for zeolite thermodynamics by enabling reliable thermochemical data on natural zeolites of geochemical importance and synthetic pure zeolites applied in the petrochemical industry as sorbents, ion-exchange media, and catalysts. Nevertheless, thermodynamics of zeolites with encapsulated heterocore TM species, such as TMO, TMC, and/or TMN clusters, has not been systematically investigated and documented. Determination of the macroscopic thermodynamic parameters that govern the formation, stability, and microscopic local structures of heterocore TM species under zeolite encapsulation will lead to enhanced understanding of the design, synthesis, and applications TM-based zeolite catalysts in chemical engineering processes.

Recently, we reported an adsorption calorimetry study elucidating the *real-time* formation energetics in regeneration and thermal stability of the copper oxo clusters (CuO_x) confined within copper–mordenite (Cu–MOR), a promising low-temperature methane (CH_4) conversion catalyst, in which a rich energetic landscape is projected for zeolites with different heterocore TM species encapsulated.[42] The results also suggest that, unlike the extra-framework cations in alkali and alkaline earth ion-exchanged zeolites, once encapsulated, TMO species, such as CuO_x, may alter the oxidation state of metal, stoichiometry, and/or local structure/assemblage to achieve energetically favorable final states. The objective of this study is to determine the formation energetics and guest–host interactions and to identify the relationships among structure, distribution, and energetics of the unique molybdenum trioxide (MoO_3)–zeolite Y (faujasite or FAU) guest–host systems, in which a TMO, MoO_3, is encapsulated within the microporosity of zeolite Y with faujasite topology (FAU). Zeolite Y is selected for its compositional tunability, high crystallinity, and open supercage, which enables nanoscale internal space to host MoO_3 clusters/particles. Taking advantage of a full spectrum of calorimetric capabilities in the Alexandra Navrotsky Institute for Experimental Thermodynamics (AlexInstitute) at Washington State University (WSU), we probed the enthalpies of formation and energetics of guest–host interactions for the MoO_3–zeolite Y system employing high-temperature oxide melt solution calorimetry as the major experimental tool. Coupled with inductively coupled plasma mass spectrometry (ICP-MS), *ex situ* X-ray diffraction (XRD), transmission electron microscopy (TEM), *ex situ* diffuse reflectance infrared Fourier transform spectroscopy (DRIFTS), Raman spectroscopy, and thermal analysis using an integrated thermogravimetry–differential scanning calorimetry–mass spectrometry system (TG-DSC-MS), we elucidated the thermodynamics complexity of MoO_3 formation under zeolite Y confinement

as a function of Si/Al ratio with complimentary compositional, morphological, structural, and spectroscopic insights. Furthermore, the relations among closely balanced compositional, structural, and thermodynamic factors were discussed.

2 | EXPERIMENTAL METHODS

2.1 | Material synthesis

Commercial zeolite NH_4Y samples (Alfa Aesar) with different Si/Al ratios were used as the starting framework materials, which were calcined at 500°C for 4 h to obtain zeolite HY. Ammonium molybdate tetrahydrate (Sigma-Aldrich, 99%), the Mo precursor, was introduced into zeolite Y samples by incipient wetness impregnation (IWI). We intentionally kept the MoO_3 loading relatively low to minimize crystal growth on the external surface of FAU. Specifically, the zeolites were pretreated in a vacuum oven at 80°C for 4 h. Subsequently, 1.5 ml of ammonium molybdate aqueous solution (0.05 mol/L) was dripped onto 1 g of pretreated samples, followed by 1-h sonication at room temperature. After oven-drying at 120°C overnight and calcination in a tube furnace at 600°C in air for 10 h, the MoO_3/FAU samples were obtained. According to the Si/Al ratio (*n*) and MoO_3 encapsulation, the samples were labeled as *n*FAU and MoO_3/*n*FAU (see Table 1). For example, the MoO_3-containing zeolite Y sample with Si/Al = 3.0 was named as MoO_3/3.0FAU.

2.2 | Phase and morphology identification

Room temperature *ex situ* powder XRD was employed for phase identification using a Rigaku Miniflex 600 diffractometer operated at 40 kV and 15 mA with Cu $K\alpha$ radiation ($\lambda = 1.5406$ Å). The XRD patterns were recorded from 5° to 60° at a step of 2°/min. The sample morphology was evaluated with TEM (FEI Tecnai T20, LaB_6 cathode, 200 kV) in the Franceschi Microscopy and Imaging Center at WSU. In each TEM experiment, a small amount of specimen was dispersed in ethanol under ultrasonication. This suspension was dropped on a carbon-coated nickel grid (200 mesh), which was further dried using infrared lamp for 20 min.

2.3 | N_2 adsorption–desorption full isotherm analysis

Brunauer–Emmett–Teller (BET) surface area and Brunauer-Joyner-Halenda (BJH) pore dimension analyses were performed via N_2 adsorption–desorption full isotherm analysis at liquid nitrogen temperature (77 K or − 196 °C) using a commercial gas adsorption analyzer (Micromeritics 3Flex). Each sample was degassed at 300°C at the analysis port of 3Flex for at least 5 h before isotherm measurement.

2.4 | Compositional and thermal analyses

The sample compositions were determined with ICP-MS (Agilent 770) and an integrated TG-DSC-MS system (Netzsch STA 449 F5 Jupiter coupled with QMS 403 D Aëolos). In the thermal analysis, the sample was placed in a platinum (Pt) crucible for TG-DSC measurement from 30 to 1000°C at 10°C/min under N_2 flow of 50 ml/min. The gas phase species evolved from TG-DSC were introduced to the MS via a heated capillary tube accurately controlled at 200°C for compositional identification. We also calculated the enthalpy of dehydration of each sample based on its TG-DSC-MS data. Dehydration and potential phase transition were mirrored on the TG-DSC-MS curves (see Table S1).

2.5 | *Ex situ* DRIFTS

Ex situ DRIFTS experiments were performed on a Nicolet iS50 FT-IR instrument from Thermo Scientific. All samples were pretreated in a 120°C oven for 4 h to remove physisorbed water before DRIFTS experiments, which were performed at room temperature with data recorded from 4000 to 650 cm^{-1}.

2.6 | Raman spectroscopy

Raman spectra of all samples were collected on a Horiba LabRAM HR Raman spectrometer with Ventus LP 532-nm laser. In each

TABLE 1 Chemical composition, molecular weight, and lattice parameter of each FAU or MoO_3/FAU sample studied on TO_2 basis

Sample	Chemical composition on TO_2 basis	MW	*a* (Å)	BET surface area (m²/g)	Specific volume (m³/g)	Pore size (nm)
2.9FAU	$(SiO_2)_{0.742}(Al_2O_3)_{0.13} \cdot 0.916 H_2O$	74.23	8.2906	1067.4	0.65	0.72
16.1FAU	$(SiO_2)_{0.942}(Al_2O_3)_{0.03} \cdot 0.196 H_2O$	63.07	8.0297	1176.4	0.79	0.77
29.3FAU	$(SiO_2)_{0.967}(Al_2O_3)_{0.017} \cdot 0.136 H_2O$	62.23	8.0424	1203.9	0.72	0.78
45.6FAU	$(SiO_2)_{0.979}(Al_2O_3)_{0.011} \cdot 0.078 H_2O$	61.28	8.145	911.1	0.58	0.78
MoO_3/2.9FAU	$(MoO_3)_{0.025}(SiO_2)_{0.742}(Al_2O_3)_{0.13} \cdot 0.727 H_2O$	74.37	8.1581	703.1	0.44	0.72
MoO_3/16.1FAU	$(MoO_3)_{0.031}(SiO_2)_{0.942}(Al_2O_3)_{0.03} \cdot 0.177 H_2O$	67.24	7.9671	631.6	0.46	0.76
MoO_3/29.3FAU	$(MoO_3)_{0.027}(SiO_2)_{0.967}(Al_2O_3)_{0.017} \cdot 0.138 H_2O$	66.15	8.0297	1057.2	0.65	0.77
MoO_3/45.6FAU	$(MoO_3)_{0.027}(SiO_2)_{0.979}(Al_2O_3)_{0.011} \cdot 0.120 H_2O$	65.91	8.0424	631.6	0.43	0.77

Abbreviations: BET, Brunauer–Emmett–Teller; FAU, zeolite Y (faujasite); MoO_3, molybdenum trioxide; MW, molecular weight.

measurement, ~15 mg sample was loaded into a Linkam CCR cell, and the spectra were directly recorded at room temperature.

2.7 | Hydrogen temperature-programmed reduction

Hydrogen temperature-programmed reduction (H_2 TPR) experiments were carried out on a Diablo 5000A *real-time* gas analyzer with an Agilent 5975C MSD as the detector. Prior to the H_2 TPR analysis, each sample was pretreated *in situ* by heating to 600°C (10°C/min) in argon (Ar) flow (50 ml/min). The sample was kept at 600°C for half an hour to remove any preadsorbed species. Upon cooling to 50°C, H_2 flow (25 ml/min) was introduced, meanwhile, the Ar flowrate is adjusted to 25 ml/min. Subsequently, the sample analyzed was heated from 50 to 850°C in 80 min in the 1:1 mixture of H_2 and Ar (25 ml/25 ml). The water signal was recorded for further interpretation.

2.8 | High-temperature oxide melt drop solution calorimetry

A Tian-Calvet twin microcalorimeter (Setaram Alexsys-1000) at WSU was employed for high-temperature oxide melt drop solution calorimetry. The details of this methodology have been introduced earlier elsewhere by Navrotsky et al.[43] To measure the enthalpy of dissolution of each sample, a sample pellet (~5 mg) was directly dropped into Alexsys-1000, which contains the solvent, lead borate (2PbO·B_2O_3) molten salt at 700 °C under flowing compressed air at a rate of 120 ml/min. Such calorimetric measurement on each sample was repeated for at least six times. The calorimeter calibration was carried out by measuring the heat content of corundum (Al_2O_3). The enthalpies of formation and MoO_3–zeolite Y guest–host interactions of all samples were derived using the thermodynamic cycle listed in Table 2. The errors were calculated as two standard deviations (SDs) of the mean.

3 | RESULTS AND DISCUSSION

The compositions determined by coupled ICP-MS and TG-DSC-MS, including the formula and molecular weight of each sample on TO_2 (tetrahedron unit) basis, are summarized in Table 1. The compositional results of MoO_3/FAU suggest successful inclusion of MoO_3, and decreased water contents and molecular weight as Si/Al increases (see Table 1). The Mo/Al ratio of 2.9FAU, sample with the highest Al content, is about 0.1, and the Mo/Al ratio of 45.6FAU, sample with the lowest Al content, is ~1.2. The *ex situ* XRD patterns of all FAU and MoO_3/FAU samples collected at room temperature are shown in Figure 1A,B. The XRD results confirm that all FAU samples have cubic faujasite structure belonging to the *Fd3m* space group, and MoO_3 encapsulation does not lead to significant disturbance of the long-range order of the frameworks.[44,45] The lattice parameter of each

TABLE 2 Thermochemical cycle to calculate the enthalpies of formation (per TO_2) at 25°C of FAU and MoO_3/FAU samples from their constituent oxides and elements

$(MoO_3)_x \cdot (SiO_2)_y \cdot (Al_2O_3)_z \cdot nH_2O_{(s,25°C)}$ $\rightarrow xMoO_{3(soln.,700°C)} + ySiO_{2(soln.,700°C)}$ $+ zAl_2O_{3\ (soln.,700°C)} + nH_2O_{(g,700°C)}$	$\Delta H_1 = \Delta H_{ds}$
$MoO_{3(s,25°C)} \rightarrow MoO_{3(soln.,700°C)}$	ΔH_2
$SiO_{2(s,25°C)} \rightarrow SiO_{2(soln.,700°C)}$	ΔH_3
$Al_2O_{3(s,25°C)} \rightarrow Al_2O_{3(soln.,700°C)}$	ΔH_4
$H_2O_{(l,25°C)} \rightarrow H_2O_{(g,700°C)}$	ΔH_5
$Mo_{(s,25°C)} + 3/2O_{2(g,25°C)} \rightarrow MoO_{3(s,25°C)}$	ΔH_6
$Si_{(s,25°C)} + O_{2(g,25°C)} \rightarrow SiO_{2(s,25°C)}$	ΔH_7
$2Al_{(s,25°C)} + 3/2O_{2(g,25°C)} \rightarrow Al_2O_{3(s,25°C)}$	ΔH_8
$(MoO_3)_x \cdot (SiO_2)_y \cdot (Al_2O_3)_z \cdot nH_2O_{(s,25°C)}$ $\rightarrow (MoO_3)_x \cdot (SiO_2)_y \cdot (Al_2O_3)_{z(s,25°C)}$ $+ nH_2O_{(l,25°C)}$	ΔH_9
$(MoO_3)_x \cdot (SiO_2)_y \cdot (Al_2O_3)_{z(s,25°C)} \rightarrow$ $xMoO_{3(soln.,700°C)} + ySiO_2$ $_{(soln.,700°C)} + zAl_2O_{3(soln.,700°C)}$	$\Delta H_{10} = \Delta H_{ds,correct}$
$\Delta H_{ds,correct} = \Delta H_{10} = \Delta H_1 - n\Delta H_5 - \Delta H_9$	
$xMoO_{3(s,25°C)} + ySiO_{2(s,25°C)} + zAl_2O_{3(s,25°C)}$ $\rightarrow (MoO_3)_x \cdot (SiO_2)_y \cdot (Al_2O_3)_{z(s,25°C)}$	$\Delta H_{11} = \Delta H_{f,ox}$
$\Delta H_{f,ox} = \Delta H_{11} =$ $x\Delta H_2 + y\Delta H_3 + z\Delta H_4 - \Delta H_{10}$	
$xMo_{(s,25°C)} + ySi_{(s,25°C)} + 2zAl_{(s,25°C)} + (3x+2y$ $+3z)/2O_{2(g,25°C)} \rightarrow (MoO_3)_x \cdot (SiO_2)_y \cdot (Al_2O_3)_z$ $_{(s,25°C)}$	$\Delta H_{12} = \Delta H_{f,el}$
$\Delta H_{f,el} = \Delta H_{12} = x\Delta H_6 + y\Delta H_7$ $+ z\Delta H_8 + \Delta H_{11}$	
$xMoO_{3(s,25°C)} + (SiO_2)_y \cdot (Al_2O_3)_{z(s,25°C)} \rightarrow$ $(MoO_3)_x \cdot (SiO_2)_y \cdot (Al_2O_3)_{z(s,25°C)}$	$\Delta H_{13} = \Delta H_{inter}$
$\Delta H_{inter} = \Delta H_{13} = \Delta H_{12,MoO_3/FAU} -$ $\Delta H_{12,FAU} - x\Delta H_6$	

Abbreviations: BET, Brunauer–Emmett–Teller; FAU, zeolite Y (faujasite); MoO_3, molybdenum trioxide; MW, molecular weight.

sample is calculated and listed in Table 1 (also see Figure 1C). For both FAU and MoO_3/FAU, as the Si/Al ratio increases, the parameter tends to decrease until reaching a plateau at about 8 Å. Meanwhile, MoO_3 loading results in slightly decreased a parameter by ~1% (Figure 1C). This set of structural evidence suggests that encapsulation of MoO_3 clusters does not result in significant modification or interruption on the framework structure of zeolite Y over a wide Si/Al range. In addition, our results also indicate that standard XRD cannot detect the encapsulated MoO_3 clusters, evidenced by the absence of any detectable diffraction patterns of MoO_3.

The TEM images of all samples are assembled in Figure 1D–K. All FAU samples feature octahedral configuration with sharp-edged crystal-like morphology.[46,47] It appears that the particle size of zeolite Y in our study spans from 400 to 600 nm. Owing to the high thermal stability of FAU, after impregnation with Mo precursor and calcination at 600°C for 10 h, there is no significant morphological degradation detected on all MoO_3/FAU samples. Interconnected nano-sized
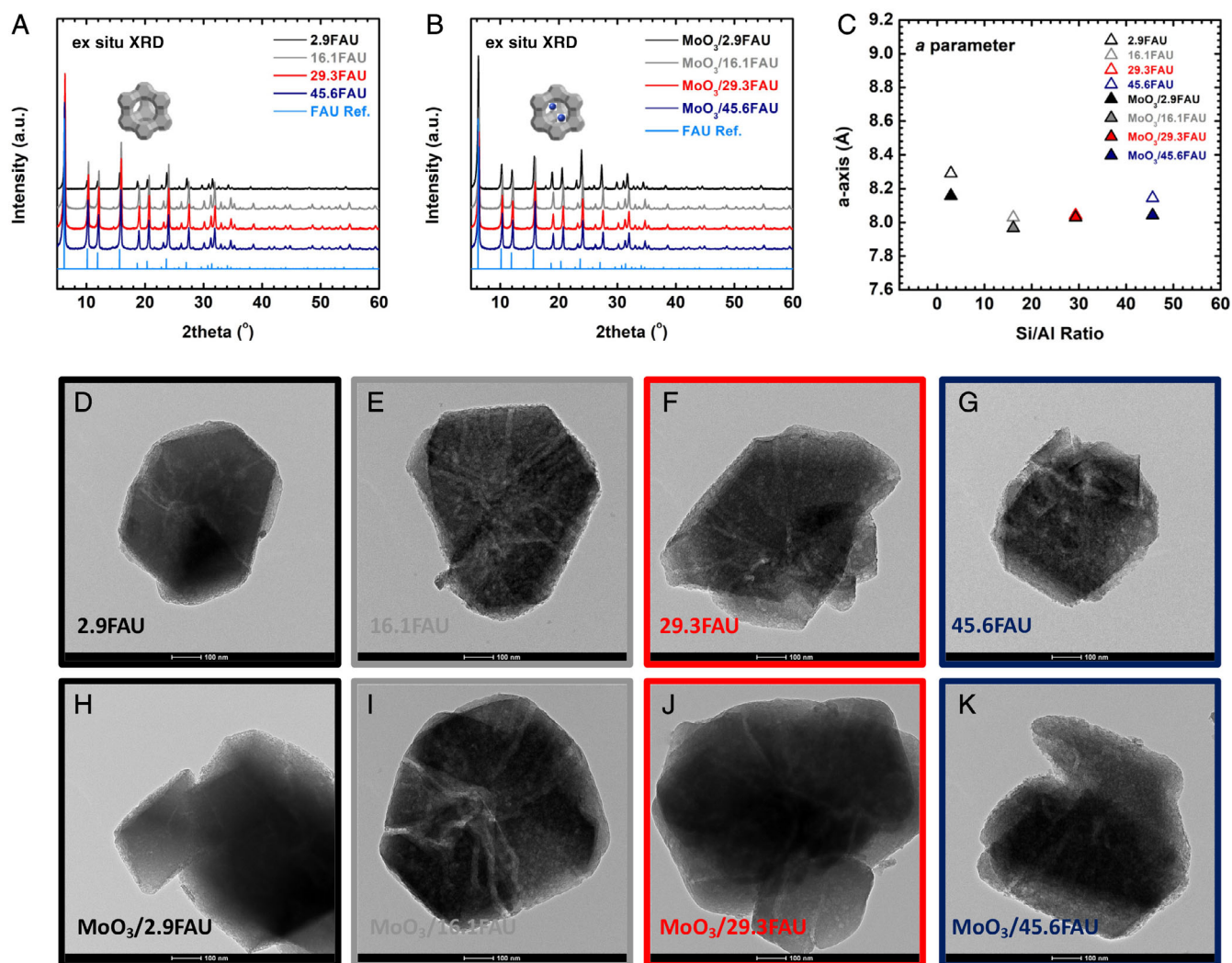
FIGURE 1 Structural illustration and *ex situ* XRD patterns of **(a)** FAU and **(b)** MoO$_3$/FAU, and **(c)** the a parameter of each sample as a function of Si/Al ratio. All XRD patterns were collected at room temperature. The reference patterns of FAU are also included. **(d–k)** The TEM images of all samples. The scale bar of each TEM image is 100 nm

channels are clearly observed within these FAU crystals, which remain very well preserved after MoO$_3$ encapsulation. We also noticed that the samples with higher Si content than that of 2.9FAU tend to feature more interconnected nanochannels. Moreover, according to the TEM images, there is no observable MoO$_3$ particle on the external surface of FAU containing MoO$_3$. This is strong evidence suggesting that the MoO$_3$ particles/clusters are dispersed within the FAU frameworks. Thus, integrating the compositional, structural, and morphological results, we conclude that the majority of the population of MoO$_3$ clusters introduced are successfully encapsulated within the crystalline framework and nanoscale porosity of each FAU sample.

The N$_2$ adsorption–desorption isotherms of all samples are plotted in Figure 2A,B. The BET specific surface areas are 1067.4, 1176.4, 1203.9, and 911.1 m^2/g for 2.9FAU, 16.1FAU, 29.3FAU, and 45.6FAU, respectively. Generally, MoO$_3$ encapsulation decreases the surface of FAU, and the specific areas are determined to be 703.1 m^2/g for MoO$_3$/2.9FAU, 631.6 m^2/g for MoO$_3$/16.1FAU,

1057.2 m^2/g for MoO$_3$/29.3FAU, and 631.6 m^2/g for MoO$_3$/45.6FAU. The pore size distribution plots are presented in Figure 2C,D. The common behavior is that the pore volume of each FAU sample decreases upon the introduction of MoO$_3$, and the pore size ranges from 0.72 to 0.78 nm (see Table 1). As demonstrated in the TEM images, there is nano-sized porosity/channel for each FAU or MoO$_3$/FAU sample. Inclusion of MoO$_3$ does not lead to significant channel blockage, and there is no detectable bulk MoO$_3$ formation on the external surface of zeolite Y or FAU (see Figures 1 and 2).

The interfacial chemistry and MoO$_3$–zeolite Y bonding specifics of all samples were studied by *ex situ* DRIFTS (see Figure 3A–D). Fundamentally, the low wavenumber absorbance of bonds within MoO$_3$ appears to be weak. Si/Al ratio increase leads to decreased local hydrophilicity within zeolite Y, evidenced by clearly observed intensity decrease in peaks between 3700 and 3000 cm^{-1}, and at 1640 cm^{-1}, corresponding to the stretching vibration of O—H groups and bending vibration of H$_2$O molecules, respectively.[42,48,49] More specifically, for
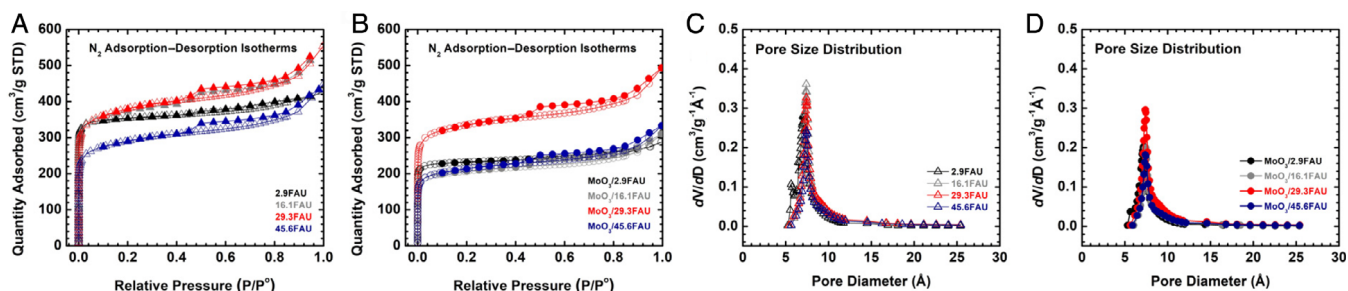
FIGURE 2 N_2 adsorption–desorption isotherms of **(a)** FAU and **(b)** MoO_3/FAU measured at 77 K ($-196°C$), and corresponding pore size distribution plots of **(c)** FAU and **(d)** MoO_3/FAU
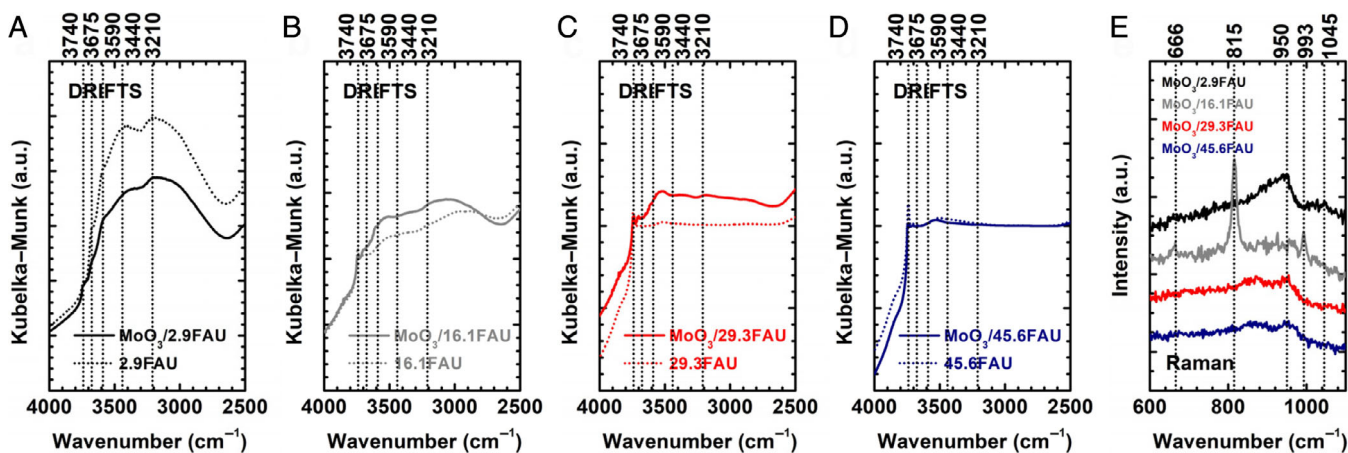
FIGURE 3 **(a–d)** *Ex situ* diffuse reflectance infrared Fourier transform spectroscopy (DRIFTS) data of all FAU and MoO_3/FAU samples. The sample names are labeled in each figure, and **(e)** Raman spectroscopy results of MoO_3/FAU

2.9FAU, MoO_3 encapsulation results in decreased intensity of peaks at 3640 cm^{-1} (shoulder) and 3545 cm^{-1} (shoulder) both ascribed to the stretching vibration of O—H bond of H_2O adsorbed at the Brønsted acid sites, and absorbance at 3440 (broad) cm^{-1} and 3210 cm^{-1} (broad) which are assigned to hydroxyl groups of water clusters, whereas the intensity of peak at 3740 cm^{-1} corresponding to stretching vibration of isolated silanol (Si—OH) groups does not change (Figure 3A).[50,51] In contrast, for the other FAU samples, the isolated silanol peak at 3740 cm^{-1} decreases upon MoO_3 introduction. In other words, the MoO_3 clusters on 2.9FAU are very likely anchored at the Brønsted acid sites near Al^{3+}. In contrast, for FAU samples with higher Si contents equal or higher than Si/Al = 16.1, MoO_3 tends to interact with a full spectrum of energetically distinctive sites closed to Si atoms because of much lower Al^{3+} concentration. Indeed, such selective binding of MoO_3 at or near Al^{3+} sites was also reported for encapsulation of MoO_3 in zeolites with other topologies and Si/Al ratios, such as ZSM-5.[50,51] Hence, evidence from DRIFTS suggests the presence of well-dispersed MoO_3 particles bonded near Al—OH in 2.9FAU, the sample with higher Al content and crystallinity (see Figure 1A), while for high silica FAU samples it is likely that there are multiple MoO_3 species experiencing intricate local chemistry with a spectrum of silanol groups and the pore structures. More specifically, when the zeolite is Al rich, such as the sample

2.9FAU, Brønsted acid sites dominate the binding, reflected by the decrease of absorbance intensity at 3640 and 3545 cm^{-1}, corresponding to bridged hydroxyl groups (Brønsted acid sites) located at the supercage and sodalite cages, respectively.[52,53] On the other hand, the distribution of MoO_3 binding sites on Si-rich zeolites is more complicated with much higher heterogeneity. For example, Tsutsumi et al. employed energy-level function derived from experimental heat function to investigate the surface heterogeneity of zeolite NaY.[54] Their study suggested that there were at least five types of silanol sites on zeolite NaY.[54] Parallely, Hattori et al. studied the silanol groups on dealuminated high silica MFI zeolite, in which they proposed four types of silanols: isolated silanol, terminal silanols, including geminal and vicinal silanol, and silanol nest.[55] Moreover, Carlos et al. employed density functional theory (DFT) method to understand the silanol chemistry of aluminum (Al)-substituted MFI nanosheets.[56] They proposed two additional types of silanols: (i) silanols with silicon directly bonds aluminum through non-protonated oxygen, and (ii) silanols whose silicon is connected to the aluminum via protonated oxygen.[56] Therefore, it is clear that the bonding distribution of MoO_3 on high silica zeolites is much more complex compared with its chemistry on zeolites rich in aluminum.

The Raman spectroscopy results are presented in Figure 3E, which further confirm the conclusion based on DRIFTS data by

presenting a set of peaks reflecting the degree of dispersion and symmetry for MoO_3 particles. The weak single Raman band at ~993 cm^{-1}, seen on all MoO_3/FAU samples, is attributed to the Mo≡O stretching.[57] The presence of a broad shoulder band at about 950 cm^{-1} for each MoO_3/FAU suggests that there are well-dispersed MoO_3 species at the vacancy defects of FAU framework.[57] Interestingly, for MoO_3/16.1FAU, well-resolved bands at 815 and 666 cm^{-1} were observed, which indicate the existence of nano-sized crystalline particles in addition to well-dispersed α-MoO_3.[57–60] Such particles around 1 nm are commonly seen for zeolites with 12-member rings and nanochannels, such as FAU, which features supercage and nanoscale porosity.[57–60] Since there is no observable large MoO_3 particles residing on the external surface of all samples, majority of MoO_3 nanoparticles are considered to be hosted in the internal space, crystalline framework, and/or nanochannels, of FAU. Meanwhile, we also found evidence suggesting the presence of —$Al_2(MoO_4)_3$ clusters in MoO_3/2.9FAU, the sample with the highest Al content, according to a weak band barely resolved at about 1045 cm^{-1}.[57,58,60] However, such —$Al_2(MoO_4)_3$ clusters or smaller particles were not detected on other MoO_3/FAU samples with higher Si content. This phenomenon highlights the strong MoO_3–zeolite Y interactions with defined interfacial bonding at the Al atoms of AlO_4 tetrahedra. In general, the Raman spectroscopy results synchronize well with the DRIFTS data, both suggesting dispersed MoO_3 particles encapsulated in the FAU frameworks. The MoO_3–FAU interfacial bonding specifics, degree of dispersion, and symmetry for encapsulated MoO_3 particles depend on the Si/Al ratio.

To reveal the influence of Si/Al ratio on the oxygen donation capability of encapsulated MoO_3 species, MoO_3 dispersion, and MoO_3–zeolite Y interactions, H_2 TPR experiments were carried out on all MoO_3/FAU samples, in which the signal of reduction product, H_2O, was simultaneously monitored as a function of temperature (see Figure 4A). Generally, weak TPR signals were seen on all MoO_3/FAU samples. To validate that these broad peaks are due to reduction of

the little amount of encapsulated MoO_3 species, we performed three TPR control experiments with the same program on (i) pure 16.1FAU, (ii) physical mixture of bulk MoO_3 and 16.1FAU with 5 Mo-wt%, and (iii) physical mixture of bulk MoO_3 and 16.1FAU with 50 Mo-wt%. In Figure 4B, for each control sample, the water peak at about 100°C is owing to low temperature dehydration of the FAU framework. The well-resolved MS signals peaked at 470 and 640°C, not seen on pure 16.1FAU, are due to stepwise reduction of molybdenum trioxide, from MoO_3 to metallic Mo.[61–63] We also noticed that as the Mo content decreases from 50 to 5 Mo-wt%, the intensities of these two peaks significantly decrease. The peaks of the control sample with 5 Mo-wt% have comparable intensities as those of MoO_3/16.1FAU, and are much stronger than those of pure 16.1FAU. The results of the TPR control experiments are strong evidence confirming that the weak TPR signals observed on MoO_3/FAU samples in Figure 4A are not simply noise. Specifically, there is a main reduction peak on all MoO_3/FAU samples studied spanning from 440 to 550°C. Typically, this H_2O peak is considered to be the product of serial MoO_3 reduction in H_2 flow forming MoO_2 and H_2O.[61–63] In addition, the slight "baseline shift" observed at temperatures higher than 525°C probably indicates gradual further reduction of Mo species. We also noticed that as the Si/Al increases the reduction temperature of MoO_3 gently shifts to lower temperature. For MoO_3/2.9FAU, the reduction peak centers at ~520°C, while the other MoO_3/FAU samples have peaks at lower temperatures, 504°C for MoO_3/16.1FAU, 502°C for MoO_3/29.3FAU, and 500°C for MoO_3/45.6FAU. Besides, the water peaks appear to be widening as Si/Al increases, implying broader MoO_3 particle distribution on high silica FAU samples, which is consistent with the Raman spectroscopy data. These phenomena indicate that as the framework Al content increases, the MoO_3 clusters are energetically better stabilized by the FAU framework, leading to higher reduction resistance and evidenced by the increased onset reduction temperature. In other words, the magnitudes of MoO_3–zeolite Y interactions impact the onset reduction temperature of MoO_3 species.[61,62] The energetics of
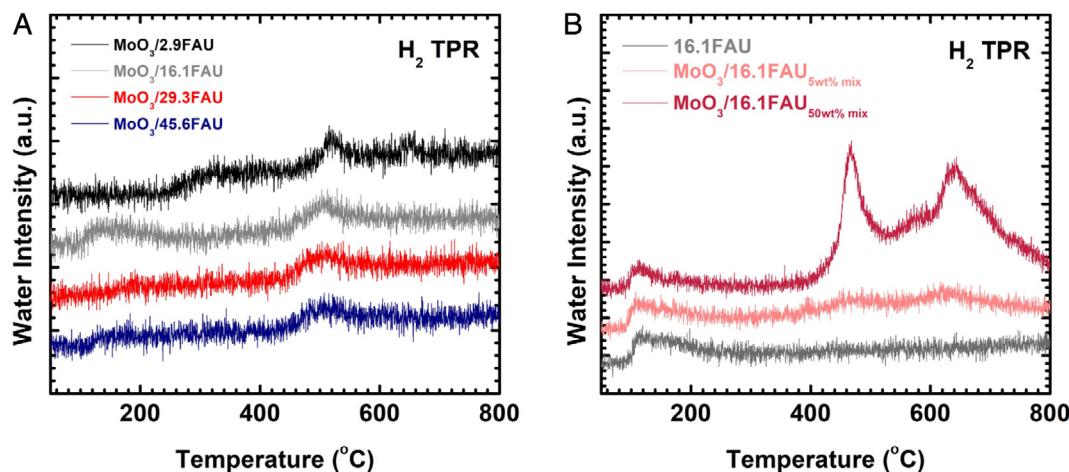

FIGURE 4 H_2 TPR results of **(a)** MoO_3/FAU samples, and **(b)** control experiments on pure 16.1FAU, physical mixture of bulk MoO_3 and 16.1FAU with Mo content of 5 and 50 Mo-wt%

MoO_3 encapsulation in all FAU frameworks is the topic we will discuss in the final section of this paper. Indeed, similar phenomena were also reported for MoO_3 supported on zeolites with other topologies and Si/Al ratios.[63] We hesitate to quantify the MoO_3 loading using H_2 TPR because of the low signal-to-noise ratio seen in Figure 4A.

The TG-DSC-MS thermal analysis results are plotted in Figure 5. The DTG and DDSC data are presented in Figures 6 and 7. Each sample features a single-step dehydration followed by calorimetric events that do not lead to observable weight loss. Specifically, the TG-DSC-MS results of FAU are relatively straightforward (Figures 5A–C, and 6A,C). All FAU samples present a single-stage weight loss due to dehydration centered at about 145°C, after which the TG-DSC-MS, DTG, and DDSC profiles are nearly featureless. The total weight losses for FAU samples range from 20.3% for 2.9FAU to 1.7% for 45.6FAU, decreasing as the Si/Al or hydrophobicity increases. Based on the DSC peak area and corresponding weight loss of each sample, the directly calculated dehydration energies from DSC are endothermic: 67.9 ± 2.1 kJ/mol H_2O for 2.9FAU, 97.0 ± 0.8 kJ/mol H_2O for 16.1FAU, 109.8 ± 3.9 kJ/mol H_2O for 29.3FAU, and 176.1 ± 4.0 for 45.6FAU. According to the XRD patterns in Figure 8A, all postanalysis FAU samples maintain their framework structure with 2.9FAU exhibiting noticeable partial degradation.

For all MoO_3/FAU samples, dehydration, concluded at temperatures below 300°C, is responsible for major weight loss. The desorbed water is 17.3% for MoO_3/2.9FAU, 4.5% for MoO_3/16.1FAU, 3.7% for MoO_3/29.3FAU, and 3.2% for MoO_3/45.6FAU (see Figures 5D and 6B). According to the TG-DSC traces, the directly calculated energies

of dehydration from DSC are 75.6 ± 3.8 kJ/mol H_2O for MoO_3/2.9FAU, 107.9 ± 1.7 kJ/mol H_2O for MoO_3/16.1FAU, 99.4 ± 2.9 kJ/mol H_2O for MoO_3/29.3FAU, and 98.5 ± 3.9 kJ/mol H_2O for MoO_3/45.6FAU. Moreover, the dehydration energies here were directly calculated by integrating the DSC curve of each sample, from zeolite-adsorbed and confined water to water vapor at elevated temperature in DSC. Such calculation introduces significantly more endothermic heat effects to the dehydration energies. Thus, we applied a thermochemical cycle (see Table S1) to correct the dehydration energies to be "dehydration enthalpies" at 25°C. The corrected dehydration enthalpies ($\Delta H_{\text{del,l}}$) range from 14.9 ± 2.1 kJ/mol H_2O for 2.9FAU to 88.9 ± 4.0 kJ/mol H_2O for 45.6FAU, and from 19.3 ± 3.9 kJ/mol H_2O for MoO_3/45.6FAU to 38.9 ± 1.7 kJ/mol H_2O for MoO_3/16.1FAU. Moreover, in principle, the enthalpy of dehydration is the average of all heat effects for water removal from a unit molar of sample with a unit of "kJ/mol H_2O." The nanoscale porosity of Al-rich zeolites can hold substantial amount of pore-confined water. These water molecules are space-fillers that are liquid-like in zeolites with hydrophilic frameworks, and do not directly bind the surface groups of zeolites. In contrast, although the internal surfaces of Si-rich zeolites are mostly hydrophobic, which adsorb much less amount of water. Most of these water molecules directly bind the surface hydroxyls of zeolites. Therefore, the dehydration enthalpies of FAU and MoO_3/FAU with higher Si/Al ratios appear to be more endothermic than those of Al-rich FAU, which confine large water clusters filling the pores. In addition, it is also such confinement-related "averaging effect" leads to comparable dehydration enthalpies for FAU and MoO_3/FAU with the same Si/Al
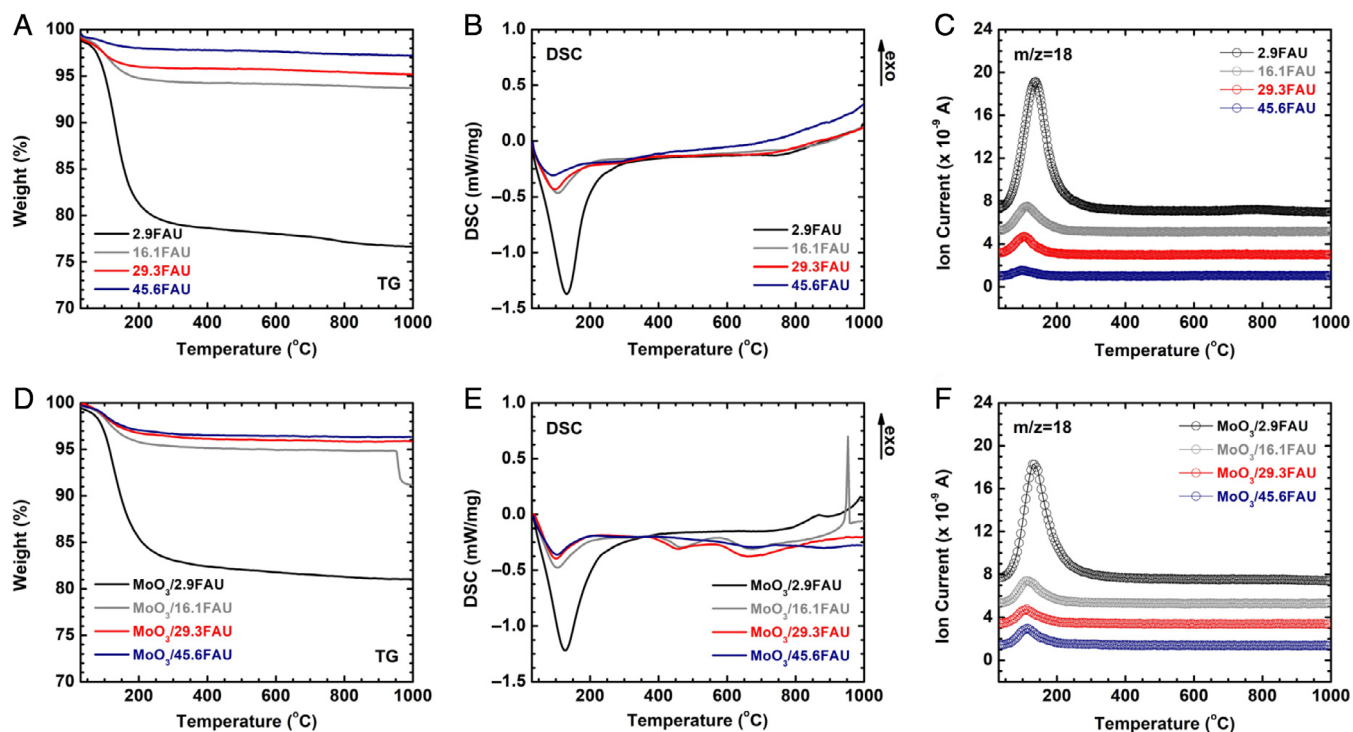
FIGURE 5 The thermal analysis results of FAU **(a)** TG, **(b)** DSC, and **(c)** MS (m/z = 18); and MoO_3/FAU **(d)** TG, **(e)** DSC, and **(f)** MS (m/z = 18) with N_2 flow at 50 ml/min from 30 to 1000°C
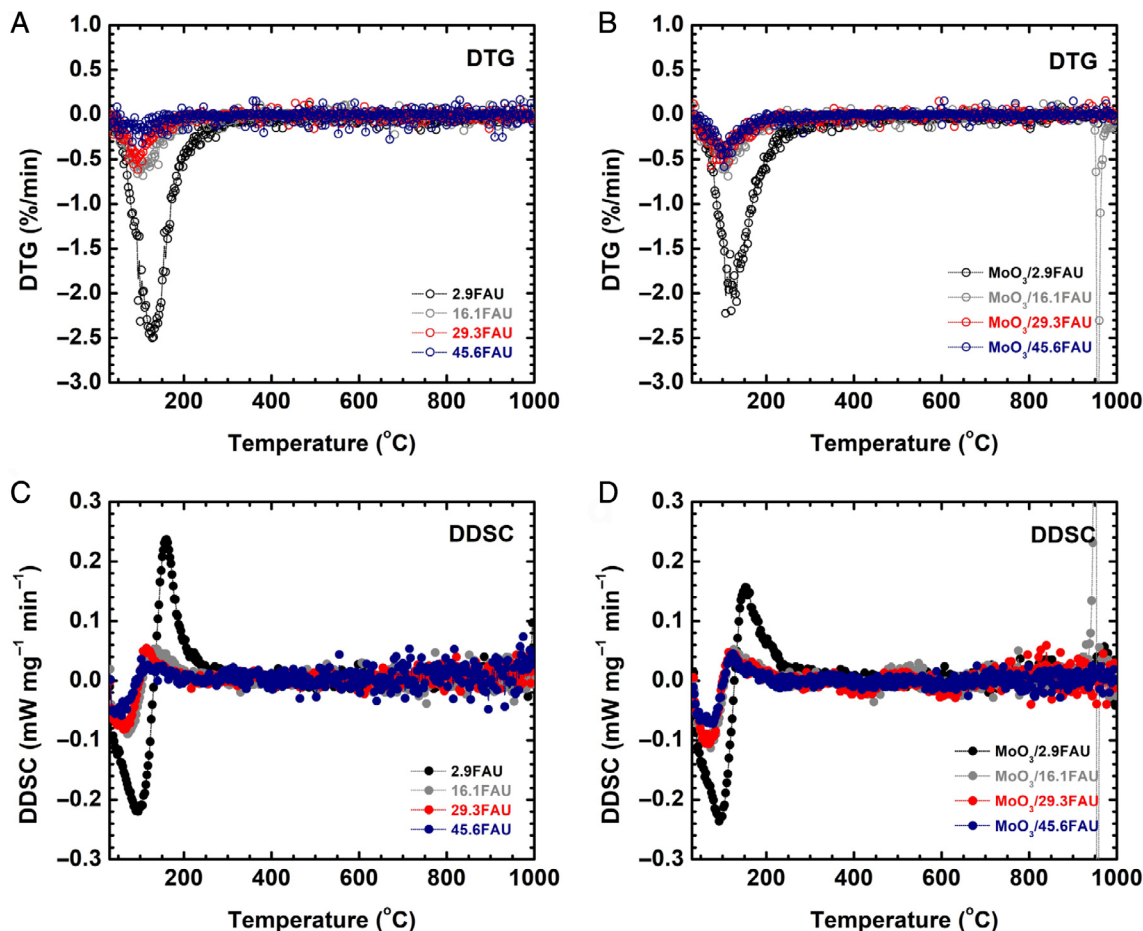
FIGURE 6 The derivative TG (DTG) profiles of **(a)** FAU and **(b)** MoO_3/FAU; and derivative DSC (DDSC) results of **(c)** FAU and **(d)** MoO_3/FAU with N_2 flow at 50 ml/min from 30 to 1000°C. [Corrections added on 23 October after online publication: The word 'differential' have been replaced with the word 'derivative'.]
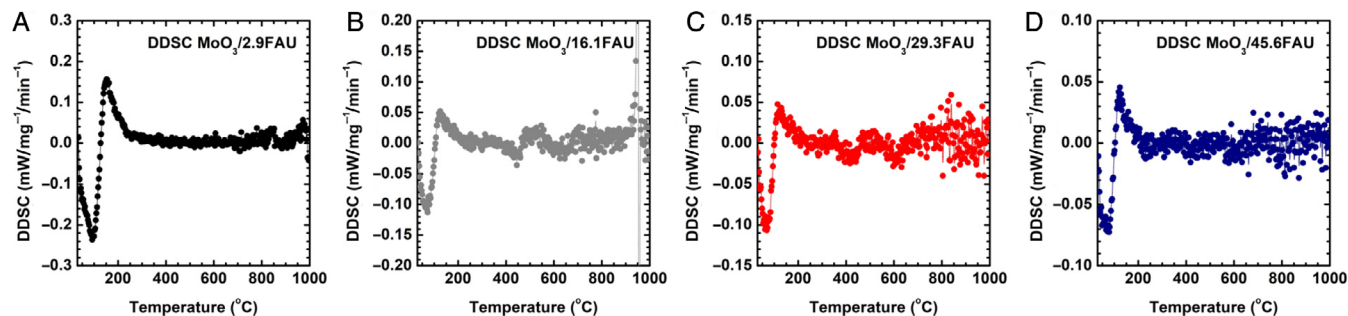
FIGURE 7 The highlighted derivative DSC (DDSC) profiles of MoO_3/FAU with N_2 flow at 50 ml/min from 30 to 1000°C, **(a)** MoO_3/2.9FAU, **(b)** MoO_3/16.1FAU, **(c)** MoO_3/29.3FAU, and **(d)** MoO_3/45.6FAU. [Corrections added on 23 October after online publication: The word 'differential' have been replaced with the word 'derivative'.]

ratio. Indeed, similar phenomena of (de)hydration energetics have been observed by Navrotsky et al. in multiple studies on zeolites, particularly, on ion-exchanged zeolites with multivalent cations, where the (de)hydration enthalpy is not a clear function of Si/Al ratio.[26,31,38,39,43] They also figured out that (de)hydration enthalpy is also governed by the degree of hydration and other guest species like cations and small organics.[26,31,38,39,43]

Interestingly, although there is no significant weight loss on the TG profiles from 300 to 900°C for all samples, a pair of broad endothermic calorimetric peaks is observed centered at about 450 and 645°C on the DSC curves of MoO_3/16.1FAU, MoO_3/29.3FAU, and MoO_3/45.6FAU, nearly consistent with the MoO_3 thermal reduction temperatures under H_2 TPR conditions (Figures 4, 5E, and 6D). We noticed that although these two peaks
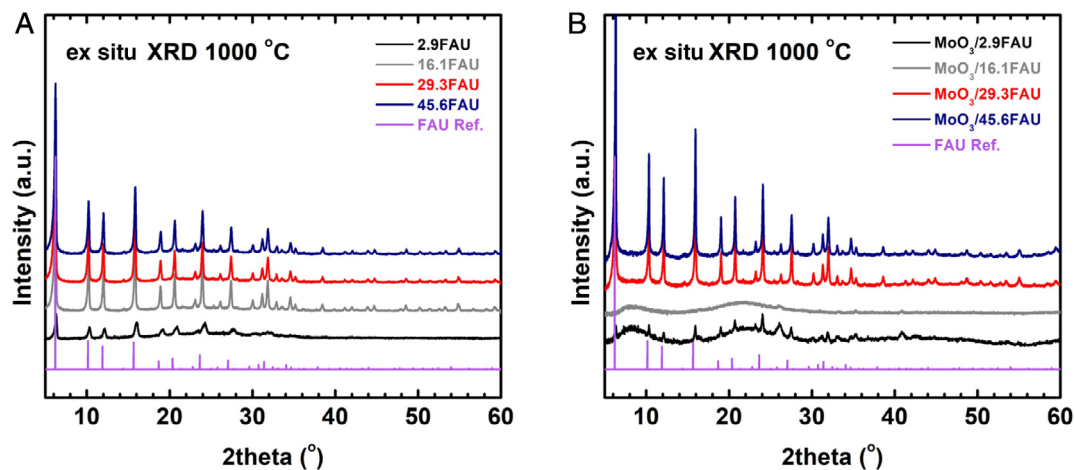
FIGURE 8 *Ex situ* XRD patterns of **(a)** FAU and **(b)** MoO_3/FAU treated at 1000°C in N_2 flow at 50 ml/min. The reference patterns of FAU are included

appear to be poorly resolved on the DSC curves of MoO_3/45.6FAU, the DDSC traces clearly reveal their trends (see Figures 6 and 7). Nevertheless, without the presence of any detectable volatile thermal reduction products evidenced by MS, such as water (m/z = 18) or O_2 (m/z = 32), we hesitate to conclude that the pair of DSC signals originates from stagewise thermal reduction of MoO_3 in non-oxidative environments (see Figures 5 and S1).[42,64] In this case, we argue that, from a thermodynamic perspective, other than redox reactions, it is possible that the endothermic peak at ~450°C is due to short-range structural transition of Mo species to reach the local assemblages with the lowest energetic states.[65,66] On the other hand, considering the melting point of bulk MoO_3 (802°C) and "melting point depression"—a common phenomenon seen for confined solid-state guest materials, we deduce, it is also possible that the second endothermic DSC peak at about 645°C could be attributed to melting of encapsulated subnano MoO_3.[35,67] We have documented similar decreased solid–liquid phase transition temperature in an earlier study on confinement of organic solid in mesoporous silicas with different pore dimensions.[35] In addition, we also noticed that the endothermic DSC peak at ~450°C appears to be absent for MoO_3/2.9FAU. We attribute that it is probably because the strong MoO_3–zeolite Y interactions on Al-rich 2.9FAU thermodynamically hinder the unfavorable redox or local structural transition of encapsulated MoO_3. Surprisingly, a sharp exothermic peak is observed on the DSC curve of MoO_3/16.1FAU at about 930°C, associated with significant weight loss as much as ~4.0%. Based on the *ex situ* XRD patterns in Figure 8**b**, suggesting completely amorphous phase for MoO_3/16.1FAU after this exothermic peak, we conclude that after melting, the Mo species evaporate, and escape zeolite Y confinement leading to eventual collapse of the framework structure, which is highly exothermic. The coexistence of exothermic DSC peak and significant weight loss reflecting vaporization of Mo species indicates the strong MoO_3–zeolite Y guest–host interactions. For MoO_3/2.9FAU, the slightly exothermic calorimetric peak at about 875°C is indicative of partial phase degradation of zeolite Y, confirmed by the XRD patterns of post DSC analysis

TABLE 3 Enthalpies of drop solution for constituent oxides and water in molten lead borate at 700°C and their enthalpies of formation from elements at 25°C

Oxide	ΔH_{ds} (kJ/mol)	$\Delta H_{f,el}$ (kJ/mol)
Corundum (Al_2O_3)	107.4 ± 0.2[43]	-1675.7 ± 1.3[71]
Molybdenum trioxide (MoO_3)	-17.8 ± 0.4 (this work)	-745.2 ± 0.4[71]
Quartz (SiO_2)	39.4 ± 0.4[43]	-910.7 ± 1.0[71]
Water (H_2O)	68.9 ± 0.1[71]	-285.8 ± 0.1[71]

sample (see Figure 8**b**), suggesting MoO_3/2.9FAU is partially amorphized. Such intricate guest–host interactions between TMO clusters and zeolites were also seen in our study on Cu oxo cluster (CuO_x) encapsulated in MOR, a low-temperature methane conversion catalyst, in which thermal decomposition of CuO_x were recorded at about 915°C, liberating molecular oxygen, resulting in a similar weak exothermic DSC peak, and leading to amorphized MOR framework.[42]

High-temperature oxide melt drop solution calorimetry, which can be used to measure the heat content of the sample plus its heat of dissolution and/or any other reactions at the temperature of solvent hosted in the calorimeter, is a powerful methodology to determine the formation enthalpies of solid-state materials at room temperature.[43,68–70] More specifically, in this study, the sample pellet, about 5 mg, was dropped from ambient condition at room temperature into the molten salt solvent (lead borate, $2PbO \cdot B_2O_3$) kept in a twin Calvet-type calorimeter (Setaram Alexsys-1000) at high temperature (700°C) under air flow (120 ml/min). The subtle difference in temperature caused by dropping, sample temperature increase, and phase transition, reaction and/or dissolution in the solvent is detected by the thermopiles, monitored by the computer program, and converted to real heat output reflecting heat of drop solution by a calibration factor predetermined.[70] Using appropriate thermochemical

TABLE 4　Enthalpies of drop solution (ΔH_{ds}) and formation enthalpies from oxides ($\Delta H_{f,ox}$) and elements ($\Delta H_{f,el}$) at 25°C (per TO_2) of all samples

Sample	ΔH_{ds} (kJ/mol TO_2)	$\Delta H_{f,ox}$ (kJ/mol TO_2)	$\Delta H_{f,el}$ (kJ/mol TO_2)	$\Delta H_{deh,l}$ (kJ/mol H_2O)	ΔH_{inter} (kJ/mol MoO_3)
2.9FAU	50.3 ± 4.0	69.7 ± 4.1	−822.1 ± 2.0	14.9 ± 2.1	N/A
16.1FAU	19.0 ± 0.3	40.8 ± 0.3	−865.7 ± 0.2	30.9 ± 0.8	N/A
29.3FAU	13.6 ± 0.8	40.8 ± 0.8	−867.5 ± 0.4	37.7 ± 3.9	N/A
45.6FAU	14.7 ± 1.1	32.8 ± 1.1	−871.9 ± 0.8	88.9 ± 4.0	N/A
MoO_3/2.9FAU	47.2 ± 1.7	61.1 ± 1.8	−849.1 ± 1.0	21.3 ± 3.8	−334.3 ± 102.7
MoO_3/16.1FAU	20.8 ± 1.2	38.0 ± 1.2	−891.8 ± 0.6	38.9 ± 1.7	−95.7 ± 7.5
MoO_3/29.3FAU	18.2 ± 0.5	34.3 ± 0.5	−897.8 ± 0.3	26.4 ± 2.9	−242.8 ± 4.8
MoO_3/45.6FAU	17.0 ± 1.4	32.8 ± 1.4	−896.3 ± 0.7	19.3 ± 3.9	−159.8 ± 15.4

Note: The dehydration enthalpies of each sample relative to liquid water ($\Delta H_{deh,l}$) and enthalpies of interactions (ΔH_{inter}) are also listed.
Abbreviations: FAU, zeolite Y (faujasite-type structure; MoO_3, molybdenum trioxide.

cycles, the differences in heats of drop solution are derived representing the enthalpies of reaction or formation at room temperature.[43,68–70] For example, the enthalpies of formation for all FAU and MoO_3/FAU samples from constituent oxides ($\Delta H_{f,ox}$ in Table 2) and elements ($\Delta H_{f,el}$ in Table 2) at 25°C are determined from their heats of drop solution, ΔH_{ds} in Table 2, with the thermodynamic cycle detailed in Table 2. The ΔH_{ds} and $\Delta H_{f,el}$ of all constituent oxides are referenced from previous reports (see Table 3).[43,71]

The ΔH_{ds} in molten lead borate at 700°C, and their enthalpies of formation from oxides ($\Delta H_{f,ox}$) and elements ($\Delta H_{f,el}$) at 25°C are listed in Table 4. We corrected the energetic effects of dehydration to be at 25°C ($\Delta H_{deh,l}$) using dehydration energies obtained from thermal analyses. $\Delta H_{f,ox}$ is plotted as a function of Si/Al ratio in Figure 9. In general, the measured heats of drop solution (ΔH_{ds}) are all endothermic, spanning from 50.3 ± 4.0 kJ/mol TO_2 (2.9FAU) to 13.6 ± 0.8 kJ/mol TO_2 (29.3FAU) for FAU, and from 47.2 ± 1.7 kJ/mol TO_2 (MoO_3/2.9FAU) to 13.6 ± 0.8 kJ/mol TO_2 (MoO_3/45.6FAU) for MoO_3/FAU samples. The common trend is that (i) increase in Si/Al ratio results in decreasing endothermic ΔH_{ds} until reaching ~15 kJ/mol TO_2; (ii) MoO_3 encapsulation does not significantly impacts the magnitude of ΔH_{ds}. Overall, the $\Delta H_{f,ox}$ of pure FAU frameworks are endothermic, ranging from 69.7 ± 4.1 kJ/mol TO_2 for 2.9FAU to 32.8 ± 1.1 kJ/mol TO_2 for 45.6FAU. Positive $\Delta H_{f,ox}$ values suggest the FAU samples are energetically less stable compared with their dense phase assemblages from constituent oxides, Al_2O_3, SiO_2, and water. As the Si/Al ratio increases, $\Delta H_{f,ox}$ of FAU framework becomes less endothermic, exhibiting an exponential trend which gradually levels until reaching about 30 kJ/mol TO_2 (see Figure 9). This trend is consistent with the formation thermodynamics of homogeneous acid–base ternary oxide, as seen in earlier studies on various ion-exchanged zeolites.[25,26,31,37–39] Considering that the samples we used are zeolite HY (FAU), the increased degree of metastability as Al content increases is mainly because of Al^{3+} substitution, which results in formation of negatively charged AlO_4^- tetrahedra and increased framework charge density. In Figure 9, we also plotted the formation enthalpies data of a family of ion-exchanged zeolite Y (FAU) with the same Si/Al ratio (Si/Al ~2.8) reported by Yang and Navrotsky, in which they systematically evaluated the impacts of extra-framework cations on
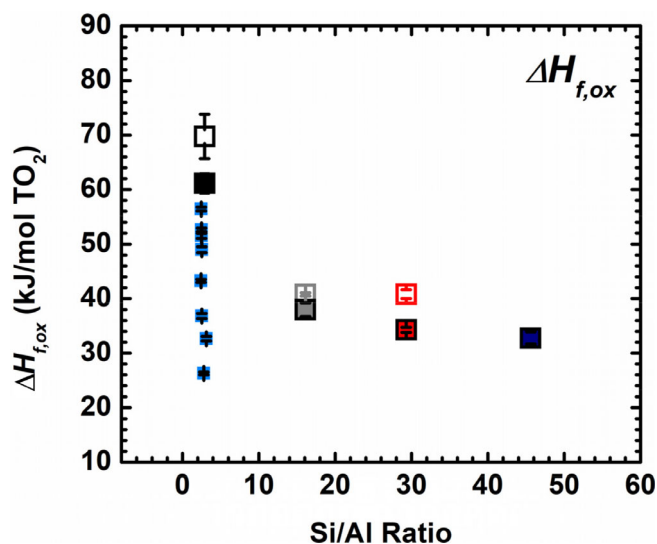
FIGURE 9　Enthalpies of formation from constituent oxides (SiO_2, Al_2O_3, and MoO_3) at 25°C (per TO_2) of all FAU and MoO_3/FAU samples. Enthalpies of formation data of ion-exchanged zeolite Y with the same Si/Al ratio (Si/Al ~ 2.8) documented by Yang and Navrotsky in 2000 are also presented (light blue squares).[31]

formation enthalpies of zeolite Y.[31] Therefore, it is clear that FAU becomes energetically less stable from constituent oxides at 25°C as the Al content or the average ionic potential increases.

On the other hand, encapsulation of MoO_3 energetically stabilizes FAU framework, supported by the less endothermic formation enthalpy of each MoO_3/FAU compared with corresponding FAU, ranging from 61.1 ± 1.8 kJ/mol TO_2 for MoO_3/2.9FAU to 32.8 ± 1.4 kJ/mol TO_2 for MoO_3/45.6FAU. Parallely, $\Delta H_{f,el}$ mimics the trend of $\Delta H_{f,ox}$ (see Table 4). Notably, compared with the magnitudes of OSDA–framework interactions, which are around 5.0 kJ/mol TO_2, confinement of MoO_3 significantly stabilizes FAU.[29] In other words, energetically favorable MoO_3 particles–FAU framework interactions through surface binding and confinement effects are expected, which

pay for the "energetic cost of being small." We estimated the enthalpies of MoO_3–zeolite Y interactions, ΔH_{inter}, in kJ/mol MoO_3, to quantify the magnitudes of energetic effects of formation of MoO_3/FAU from bulk MoO_3 and pure FAU (see Table 2). All ΔH_{inter} values are exothermic between -95.7 ± 7.5 kJ/mol MoO_3 for MoO_3/16.1FAU and -334 ± 102.7 kJ/mol MoO_3 for MoO_3/2.9FAU. Despite wide error bar originated from the cumulative errors of our stepwise calculations, the most exothermic ΔH_{inter} was observed on MoO_3/2.9FAU, which indicates significant energetic cost to stabilize the well-dispersed metastable amorphous MoO_3 clusters, while the energetically least favorable interactions were observed for MoO_3/16.1FAU, which has nanosized MoO_3 particles that probably lower the total energies through exothermic crystallization process as seen in our earlier study on confinement of organic nanocrystals.[35] Moreover, we would like to mention that the ΔH_{inter} is more exothermic than what was observed for confinement of rigid organic molecules in mesoporous silicas.[35] This is owing to the (i) strong confinement effects applied by the microporosity of zeolite Y, and the (ii) defined MoO_3—zeolite Y interfacial bonding, evidenced by the DRIFTS and Raman results. Thus, integration of these two types of strong interactions energetically stabilizes the dispersed MoO_3 clusters and is a prerequisite ensuring their activity, selectivity, and stability as the catalytic sites in CH_4 carburization to synthesize C_6H_6, as demonstrated by Gao et al. and Zheng et al. in their kinetic, spectroscopic, and computational investigations.[50,60]

In sum, this integrated structural, spectroscopic, and calorimetric study leads to the following conclusions and implications. *Firstly*, we argue that hydration thermodynamics is more complex for zeolites with encapsulated oxide particles, involving both compositional, interfacial (functional groups and defects), redox and structural factors. Typically, classic cation–framework–water interplays govern the hydration of alkali, alkaline earth and TM ion-exchanged zeolites, in which extra-framework cations, such as Na^+ and Ca^{2+}, determine the trend of hydration energetics because they are extremely hydrophilic and readily hydrated. Here, in contrast, after calcination in air at elevated temperature, the negative charges of FAU are neutralized by the strong MoO_3—zeolite Y interfacial bonding, which also anchors the MoO_3 particles. Hence, MoO_3/FAU does not exhibit substantially different average hydration energetics compared with the corresponding pure FAU sample, although the hydration thermodynamics at near-zero water coverage may be distinctively different between FAU and MoO_3/FAU. Unveiling the interfacial heterogeneity, and potential redox evolutions in hydration of MoO_3/FAU is an ongoing study in our group at WSU. *Secondly*, the nature of MoO_3—zeolite Y interfacial binding significantly differs from the cation–framework interactions in ion-exchanged zeolites, which are ionic. Multiple evidences from DRIFTS and Raman spectroscopy suggest when the FAU is Al-rich, MoO_3 is primarily anchored at or near the Brønsted acid sites, leading to energetically favorable bonds that feature more polar or ionic characteristics and higher particle dispersion. For high silica FAU, a spectrum of silanol groups would direct formation of MoO_3 particles with broader size distributions via formation of intricate interfacial bonds with more covalent nature. Thus, at a given MoO_3 loading, the Si/Al ratio of FAU plays a critical role

governing the interfacial bonding specifics, particle assemblage and dispersion, and confinement energetics of the MoO_3/FAU system. *Lastly*, the thermal analysis and formation energetics results both suggest that encapsulated TMO particles in zeolites could simultaneously alter the oxidation states of metal, local subnano-assemblages, particle sizes, and types of bonding in the synthesis and operation processes to reach the lowest energy level, particularly, for MoO_3, an oxide material with multiple phases, redox properties, and relatively low melting point. Indeed, the redox transition flexibility of MoO_3 was also highlighted by Murugappan et al. in their *operando* NAP-XPS study on hydrodeoxygenation (HDO) using MoO_3 and Mo_2C.[72]

4 | CONCLUSIONS

In this study, the thermodynamics of MoO_3 encapsulated in zeolite Y with different Si/Al ratios was investigated using calorimetry integrated with spectroscopic and structural methods, in which we elucidated the energetic landscape of MoO_3/FAU catalysts, potential redox and/or local structural transitions of subnano MoO_3 clusters/particles under zeolite Y confinement, and the thermodynamics–confinement–dispersion relationships. In summary, at a fixed MoO_3 loading, the redox and/or local structural transition and particle dispersion of these MoO_3/FAU catalytic materials are tightly related to the formation energetics of MoO_3/FAU and the magnitudes of MoO_3–zeolite Y interactions, which are functions of Si/Al ratio. Documentation of systematic experimental thermodynamic data on zeolite-based heterogeneous catalysts with encapsulated metal, oxides and carbides particles will aid chemical engineers and materials chemists for rational development of advanced catalytic materials using earth-abundant elements for a more sustainable future.

DATA AVAILABILITY STATEMENT

The data that support the findings of this study are available from the corresponding author upon reasonable request.

ORCID

Hui Sun https://orcid.org/0000-0002-8544-756X

Di Wu https://orcid.org/0000-0001-6879-321X

REFERENCES

1. Serna P, Gates BC. Molecular metal catalysts on supports: organometallic chemistry meets surface science. *Acc Chem Res*. 2014;47(8): 2612-2620. doi:10.1021/ar500170k
2. Guan E, Ciston J, Bare SR, et al. Supported metal pair-site catalysts. *ACS Catal*. 2020;10(16):9065-9085. doi:10.1021/acscatal.0c02000
3. Wang H, Wang L, Xiao F. Metal@Zeolite hybrid materials for catalysis. *ACS Cent Sci*. 2020;6(10):1685-1697. doi:10.1021/acscentsci.0c01130
4. Grundner S, Markovits M, Li G, et al. Single-site trinuclear copper oxygen clusters in mordenite for selective conversion of methane to methanol. *Nat Comm*. 2015;6:7546. doi:10.1038/ncomms8546
5. Wang H, Wang L, Lin D, et al. Strong metal–support interactions on gold nanoparticle catalysts achieved through Le Chatelier's principle. *Nat. Catal*. 2021;4:418-424. doi:10.1038/s41929-021-00611-3
6. Zhang C, Chen C, Dong H, Shen J-R, Dau H, Zhao J. Identification of molybdenum oxide nanostructures on zeolites for natural gas conversion. *Science*. 2015;348(6235):686-690. doi:10.1126/science.aaa7048
7. Sushkevich VL, Palagin D, Ranocchiari M, van Bokhoven JA. Selective anaerobic oxidation of methane enables direct synthesis of methanol. *Science*. 2017;356(6337):523-527. doi:10.1126/science.aam9035
8. Jin Z, Wang L, Zuidema E, et al. Hydrophobic zeolite modification for *in situ* peroxide formation in methane oxidation to methanol. *Science*. 2020;367(6474):193-197. doi:10.1126/science.aaw1108
9. Therrien AJ, Hensley AJR, Marcinkowski MD, et al. An atomic-scale view of single-site Pt catalysis for low-temperature CO oxidation. *Nat Catal*. 2018;1:192-198. doi:10.1038/s41929-018-0028-2
10. Jones J, Xiong H, DeLaRiva AT, et al. Thermally stable single-atom platinum-on-ceria catalysts via atom trapping. *Science*. 2020; 353(6295):150-154. doi:10.1126/science.aaf8800
11. Xiang Y, Kruse N. Tuning the catalytic CO hydrogenation to straight- and long-chain aldehydes/alcohols and olefins/paraffins. *Nat Commun*. 2017;7:13058. doi:10.1038/ncomms13058
12. Zhang S, Huang ZQ, Ma Y. et al. Solid frustrated-Lewis-pair catalysts constructed by regulations on surface defects of porous nanorods of CeO_2. *Nat Commun* 2017; 8: 15266. 10.1038/ncomms15266
13. Yang Z, Li H, Zhou H, et al. Coking-resistant iron catalyst in ethane dehydrogenation achieved through siliceous zeolite modulation. *J Am Chem Soc*. 2020;142(38):16429-16436. doi:10.1021/jacs.0c07792
14. Zhu J, Osuga R, Ishikawa R, et al. Ultrafast encapsulation of metal nanoclusters into MFI zeolite in the course of its crystallization: catalytic application for propane dehydrogenation. *Angew Chem Int Ed*. 2020;59(44):19669-19674. doi:10.1002/anie.202007044
15. Iida T, Shetty M, Murugappan K, et al. Encapsulation of molybdenum carbide nanoclusters inside zeolite micropores enables synergistic bifunctional catalysis for anisole hydrodeoxygenation. *ACS Catal*. 2017;7(12):8147-8151. doi:10.1021/acscatal.7b03175
16. Liu, W., You, W., Sun, W. et al. Ambient-pressure and low-temperature upgrading of lignin bio-oil to hydrocarbons using a hydrogen buffer catalytic system. *Nat Energy* 2020; 5: 759-767. 10.1038/s41560-020-00680-x
17. Zhang T. Taking on all of the biomass for conversion. *Science*. 2020; 367(6484):1305-1306. doi:10.1126/science.abb1463
18. Zhang X, Chaudhary N, Hawkins MR, et al. Determining the hydration energetics on carbon-supported Ru catalysts: an adsorption calorimetry and density functional theory study. *Catal Today*. 2021; 365(1):172-180. doi:10.1016/j.cattod.2020.09.021
19. Ding K, Gulec A, Johnson AM, et al. Identification of active sites in CO oxidation and water-gas shift over supported Pt catalysts. *Science*. 2015;350(6257):389-393. doi:10.1126/science.aac6368
20. Yao S, Zhang X, Zhou W, et al. Atomic-layered au clusters on α-MoC as catalysts for the low-temperature water–gas shift reaction. *Science*. 2017;357(6349):189-192. doi:10.1126/science.aah4321
21. Navrotsky A, Lilova K, Wu D, Asta M. Thermodynamics of complex solids. *J Mater Res*. 2019;34(19):3241-3242. doi:10.1557/jmr.2019.300
22. Davis ME, Lobo RF. Zeolite and molecular sieve synthesis. *Chem Mater*. 1992;4(4):756-768. doi:10.1021/cm00022a005
23. Navrotsky A, Trofymluk O, Levchenko AA. Thermochemistry of microporous and mesoporous materials. *Chem Rev*. 2009;109(9): 3885-3902. doi:10.1021/cr800495t
24. Petrovic I, Navrotsky A, Davis ME, Zones SI. Thermochemical study of the stability of frameworks in high silica zeolites. *Chem Mater*. 1993;5(12):1805-1813. doi:10.1021/cm00036a019
25. Hu Y, Navrotsky A, Chen CY, Davis ME. Thermochemical study of the relative stability of dense and microporous aluminophosphate frameworks. *Chem Mater*. 1995;7(10):1816-1823. doi:10.1021/cm00058a010
26. Petrovic I, Navrotsky A. Thermochemistry of Na-faujasites with varying Si/Al ratios. *Microporous Mater*. 1997;9(1–2):1-12. doi:10.1016/S0927-6513(96)00060-0
27. Piccione PM, Laberty C, Yang S, Camblor MA, Navrotsky A, Davis ME. Thermochemistry of pure-silica zeolites. *J Phys Chem B*. 2000;104(43):10001-10011. doi:10.1021/jp002148a
28. Piccione PM, Woodfield BF, Boerio-Goates J, Navrotsky A, Davis ME. Entropy of pure-silica molecular sieves. *J Phys Chem B*. 2001;105(25): 6025-6030. doi:10.1021/jp010491p
29. Piccione PM, Yang S, Navrotsky A, Davis ME. Thermodynamics of pure-silica molecular sieve synthesis. *J Phys Chem B*. 2002;106(14): 3629-3638. doi:10.1021/jp014427j
30. Yang S, Navrotsky A, Phillips BL. *In situ* calorimetric, structural, and compositional study of zeolite synthesis in the system $5.15Na_2O−1.00Al_2O_3−3.28SiO_2−165H_2O$. *J. Phys. Chem B*. 2000;104(25):6071-6080. doi:10.1021/jp9944278
31. Yang S, Navrotsky A. Energetics of formation and hydration of ion-exchanged zeolite Y. *Microporous Mesoporous Mater*. 2000;37(1–2): 175-186. doi:10.1016/S1387-1811(99)00264-4
32. Yang S, Navrotsky A, Wesolowski DJ, Pople JA. Study on synthesis of TPA-Silicalite-1 from initially clear solutions of various base concentrations by *in situ* calorimetry, potentiometry, and SAXS. *Chem Mater*. 2004;16(2):210-219. doi:10.1021/cm030587r
33. Yang S, Navrotsky A. Early-stage reactions in synthesis of TPA−silicalite-1: studies by *in situ* calorimetry, SAXS, and pH measurements. *Chem Mater*. 2004;16(19):3682-3687. doi:10.1021/cm035272q
34. Yang S, Navrotsky A. *In situ* calorimetric study of the growth of silica TPA-MFI crystals from an initially clear solution. *Chem Mater*. 2002; 14(6):2803-2811. doi:10.1021/cm0200689
35. Wu D, Hwang SJ, Zones SI, Navrotsky A. Guest–host interactions of a rigid organic molecule in porous silica frameworks. *Proc Natl Acad Sci USA*. 2014;111(5):1720-1725. doi:10.1073/pnas.1323989111
36. Sun H, Wu D, Guo X, Shen B, Liu J, Navrotsky A. Energetics of confinement of hexane in Ca–Na ion exchanged zeolite A. *J Phys Chem C*. 2014;118(44):25590-25596. doi:10.1021/jp508514e
37. Sun H, Wu D, Guo X, Shen B, Navrotsky A. Energetics and structural evolution of Na–Ca exchanged zeolite A during heating. *Phys Chem Chem Phys*. 2015;17:9241-9247. doi:10.1039/c5cp00016e
38. Sun H, Wu D, Guo X, Shen B, Navrotsky A. Energetics of sodium–calcium exchanged zeolite A. *Phys Chem Chem Phys*. 2015;17:11198-11203. doi:10.1039/c5cp01133g
39. Sun H, Wu D, Liu K, Guo X, Navrotsky A. Energetics of alkali and alkaline earth ion-exchanged zeolite A. *J Phys Chem C*. 2016;120(28): 15251-15256. doi:10.1021/acs.jpcc.6b04840

40. Yang S, Guo X, Verma A, Shiflett MB, Corbin DR, Navrotsky A. Thermochemical insights into stability and hydration of ion-exchanged zeolite ZK-5 (KFI framework). *J Phys Chem C*. 2020;124(48):26193-26202. doi:10.1021/acs.jpcc.0c06796

41. Zones SI, Jayanthi K, Pascual J, Xie D, Navrotsky A. Energetics of the local environment of structure-directing agents influence zeolite synthesis. *Chem Mater*. 2021;33(6):2126-2138. doi:10.1021/acs.chemmater.0c04796

42. Zhang X, Cockreham CB, Huang Z, et al. Thermodynamics of water-cationic species-framework guest-host interactions within transition metal ion-exchanged mordenite relevant to selective anaerobic oxidation of methane to methanol. *J Phys Chem Lett*. 2020;11(12):4774-4784. doi:10.1021/acs.jpclett.0c01331

43. Navrotsky A. Progress and new directions in calorimetry: a 2014 perspective. *J Am Ceram Soc*. 2014;97(11):3349-3359. doi:10.1111/jace.13278

44. Sang S, Liu Z, Tian P, Liu Z, Qu L, Zhang Y. Synthesis of small crystals zeolite NaY. *Mater Lett*. 2006;60(9–10):1131-1133. doi:10.1016/j.matlet.2005.10.110

45. Holmberg BA, Wang H, Yan Y. High silica zeolite Y nanocrystals by dealumination and direct synthesis. *Microporous Mesoporous Mater*. 2004;74(1–3):189-198. doi:10.1016/j.micromeso.2004.06.018

46. Janssen AH, Koster AJ, De Jong KP. Three-dimensional transmission electron microscopic observations of mesopores in dealuminated zeolite Y. *Angew Chem Int Ed*. 2001;40(6):1102-1104. doi:10.1002/1521-3773(20010316)40:6%3C1102::AID-ANIE11020%3E3.0.CO;2-6

47. De Jong KP, Zečević J, Friedrich H, et al. Zeolite Y crystals with trimodal porosity as ideal hydrocracking catalysts. *Angew Chem Int Ed*. 2010;49(52):10074-10078. doi:10.1002/ange.2010043

48. Bordiga S, Regli L, Lamberti C, Zecchina A, Bjørgen M, Lillerud KF. FTIR adsorption studies of H_2O and CH_3OH in the isostructural H-SSZ-13 and H-SAPO-34: formation of H-bonded adducts and protonated clusters. *J Phys Chem B*. 2005;109(16):7724-7732. doi:10.1021/jp044324b

49. Zecchina A, Geobaldo F, Spoto G, et al. FTIR investigation of the formation of neutral and ionic hydrogen-bonded complexes by interaction of H-ZSM-5 and H-mordenite with CH_3CN and H_2O: comparison with the H-NAFION superacidic system. *J Phys Chem*. 1996;100(41):16584-16599. doi:10.1021/jp960433h

50. Gao J, Zheng Y, Fitzgerald GB, et al. Structure of Mo_2C_x and Mo_4C_x molybdenum carbide nanoparticles and their anchoring sites on ZSM-5 zeolites. *J Phys Chem C*. 2014;118(9):4670-4679. doi:10.1021/jp4106053

51. Wang D, Lunsford JH, Rosynek MP. Characterization of a Mo/ZSM-5 catalyst for the conversion of methane to benzene. *J Catal*. 1997;169(1):347-358. doi:10.1006/jcat.1997.1712

52. Jones AJ, Iglesia E. The strength of Brønsted acid sites in microporous aluminosilicates. *ACS Catal*. 2015;5(10):5741-5755. doi:10.1021/acscatal.5b01133

53. Lakiss L, Vicente A, Gilson JP, et al. Probing the Brønsted acidity of the external surface of Faujasite-type zeolites. *ChemPhysChem*. 2020;21(16):1873-1881. doi:10.1002/cphc.202000062

54. Tsutsumi K, Mitani Y, Takahashi H. Evaluation of energy distribution on a heterogeneous surface from heat of adsorption and its application to the ammonia/Na-Y zeolite system. *Colloid Polym Sci*. 1985;263(10):838-841. doi:10.1007/BF01412962

55. Hattori H, Arudra P, Abdalla A, Aitani AM, Al-Khattaf SS. Infrared study of silanol groups on dealuminated high silica MFI zeolite to correlate different types of silanol groups with activity for conversion of 1-butene to propene. *Catal Lett*. 2020;150(3):771-780. doi:10.1007/s10562-019-02972-8

56. Hernandez-Tamargo CE, Roldan A, De Leeuw NH. A density functional theory study of the structure of pure-silica and aluminium-substituted MFI nanosheets. *J Solid State Chem*. 2016;237:192-203. doi:10.1016/j.jssc.2016.02.006

57. Lee EL, Wachs IE. *In situ* spectroscopic investigation of the molecular and electronic structures of SiO_2 supported surface metal oxides. *J Phys Chem C*. 2007;111(39):14410-14425. doi:10.1021/jp0735482

58. Lee EL, Wachs IE. Molecular design and *in situ* spectroscopic investigation of multilayered supported $M_1O_x/M_2O_x/SiO_2$ catalysts. *J Phys Chem C*. 2008;112(51):20418-20428. doi:10.1021/jp805265m

59. Tian H, Roberts CA, Wachs IE. Molecular structural determination of molybdena in different environments: aqueous solutions, bulk mixed oxides, and supported MoO_3 catalysts. *J Phys Chem C*. 2010;114(33):14110-14120. doi:10.1021/jp103269w

60. Zheng Y, Tang Y, Gallagher JR, et al. Molybdenum oxide, oxycarbide, and carbide: controlling the dynamic composition, size, and catalytic activity of zeolite-supported nanostructures. *J. Phys. Chem. C*. 2019;123(36):22281-22292. doi:10.1021/acs.jpcc.9b05449

61. Okemoto A, Harada MR, Ishizaka T, Hiyoshi N, Sato K. Catalytic performance of MoO_3/FAU zeolite catalysts modified by Cu for reverse water gas shift reaction. *Appl Catal Gen*. 2020;592:117415. doi:10.1016/j.apcata.2020.117415

62. Liu H, Xu Y. H_2-TPR study on Mo/HZSM-5 catalyst for CH_4 Dehydroaromatization. *Chinese J Catal*. 2006;27(4):319-323. doi:10.1016/S1872-2067(06)60020-X

63. Zhao K, Jia L, Wang J, Hou B, Li D. The influence of the Si/Al ratio of Mo/HZSM-5 on methane non-oxidative dehydroaromatization. *New J Chem*. 2019;43(10):4130-4136. 10.1039/C9NJ00114J

64. Spevack PA, McIntyre NS. Thermal reduction of molybdenum trioxide. *J Phys Chem*. 1992;96(22):9029-9035. doi:10.1021/j100201a062

65. Brezesinski T, Wang J, Tolbert SH, Dunn B. Ordered mesoporous α-MoO_3 with iso-oriented nanocrystalline walls for thin-film pseudo-capacitors. *Nat Mater*. 2010;9:146-151. doi:10.1038/nmat2612

66. McCarron EM III. P-MoO_3: a metastable analogue of WO_3. *J Chem Soc Chem Commun*. 1986;336-338. doi:10.1039/C39860000336

67. Cid R, Llambías FJG, Fierro JLG, Agudo AL, Vlllaseñor J. Physicochemical characterization of MoO_3-NaY zeolite catalysts. *J Catal*. 1984;89(2):478-488. doi:10.1016/0021-9517(84)90324-5

68. Navrotsky A. Progress and new directions in high temperature calorimetry. *Phys Chem Minerals*. 1977;2:89-104. doi:10.3133/b2131

69. Navrotsky A. Progress and new directions in high temperature calorimetry revisited. *Phys Chem Minerals*. 1997;24:222-241. doi:10.1007/s002690050035

70. Li G, Sun H, Xu H, Guo X, Wu D. Probing the energetics of molecule−material interactions at interfaces and in nanopores. *J Phys Chem C*. 2017;121(47):26141-26154. doi:10.1021/acs.jpcc.7b07450

71. Robie RA, Hemingway BS. *Thermodynamic Properties of Minerals and Related Substances at 298.15 K and 1 Bar (10^5 Pascals) Pressure and Higher Temperatures*. U.S. Government Printing Office; 1995. doi:10.1007/BF00307526

72. Operando NAP-XPS unveils Differences in MoO_3 and Mo_2C during Hydrodeoxygenation. *Nat. Catal*. 2018;1:960-967. doi:10.1038/s41929-018-0171-9

SUPPORTING INFORMATION

Additional supporting information may be found in the online version of the article at the publisher's website.